Chemical Engineering Journal 450 (2022) 137924

Contents lists available at ScienceDirect

Chemical Engineering Journal

journal homepage: www.elsevier.com/locate/cej

Interface engineering of high entropy Oxide@Polyaniline heterojunction enables highly stable and excellent lithium ion storage performance

Jia-Zheng Yen, Yi-Chun Yang, Hsing-Yu Tuan *

Department of Chemical Engineering, National Tsing Hua University, Hsinchu 30013, Taiwan

ARTICLE INFO

Keywords:
High-entropy oxide
Interface engineering
Polyaniline
Lithium ion battery
Energy storage

ABSTRACT

High-Entropy Oxide (HEO) is a new material system for lithium-ion battery (LIB) electrode materials; however, the poor electrical conductivity and instability of the electrode structure limit the further improvement of their electrochemical performance. In this work, we demonstrate that a highly stable and excellent Li-ion storage performance can be achieved by interfacial engineering of surface-chemically modified HEO@polyaniline heterojunctions. Polyaniline-coated HEO (HEO-MP) was prepared by polymerization of aniline on the surface of ball-milled micrometer-sized HEO (HEO-M). HEO-MP anodes exhibit high rate performance (325 mA h g^{-1} at 10 A g^{-1}) and extremely long cycling stability (261 mA h g^{-1} at 4.0 A g^{-1} after 3200 cycles), both representing the best results so far. The improved electrochemical performance can be attributed to the conductive PANI coating, which buffers volume changes and maintains structural integrity during cycling, prevents side reactions between electrolyte and electrode materials, suppresses overproduction of SEI, and enhances ionic/electronic transport. This work demonstrates that surface interface engineering is a key step to significantly improve the performance of HEO anodes in LIBs, which can be progressed on the road to its practical applications.

1. Introduction

Since the 1990 s, lithium ion batteries (LIBs) have been marketed with an architecture using graphite as the anode and lithium cobalt oxide ($LiCoO_2$, LCO) as the cathode due to its long cycle life, high energy and power capacity, and acceptable cost [1]. However, graphite anodes in LIBs are unable to meet the ever-growing demand due to its limited theoretical capacity (372 mA h g^{-1}) and poor rate capability [2]. Owing to its high capacity (600–1200 mA h g^{-1}), abundant crustal reserves and high working potential, transition metal oxides (TMOs) have attracted a great deal of attention for high-energy LIBs since the early 2000 s [3,4,5,6]. The capacity of lithium storage in TMOs is mainly achieved through the reversible conversion reaction. The electrochemical reaction formula can be elucidated as $M_xO_y + 2yLi \leftrightarrow xM + yLi_2O$ [7,8]. In addition, the transition metal (TM) formed from the conversion reaction is an efficient electrocatalyst, which activate/promote the reversible transformation of some inorganic components in the solid electrolyte interface (SEI) to generate additional capacitance [9,10]. Recently, a series of TMO electrode materials such as Co_3O_4, ZnO, Fe_2O_3, SnO_x and $NiCo_2O_4$ have been extensively reported [11,12,13,14,15]. Unfortunately, the major hurdles for TMO anodes lie in the large volume change and poor intrinsic electronic and/or ionic conductivity.

The pioneering material system " high-entropy alloy " (HEA) invented by Yeh et al [16] in 2004 having the molar configurational entropy of high-entropy material systems calculated according to the following equation: $\Delta S_{mix} = -R\sum_{N}^{i=1} x_i ln x_i$ where R is the gas content, x_i represents the mole fractions of the metal cations, and N is the total number of cation species. Materials with $\Delta S \geq 1.5R$ are categorized as high-entropy class [17,18]. Traditionally, conventional alloys consist of one or two main elements. HEA takes advantage of high entropy, severe lattice distortion, sluggish diffusion and cocktail effect. Combining the above effects, HEA has a higher degree of fracture resistance, tensile strength, and resistance to corrosion and oxidation than conventional alloys [18]. The concept of high entropy has been applied to various materials, such as high entropy oxides, carbides, diborides, nitrides and chalcogenides, etc [19]. In 2015, high-entropy oxide (HEO) $(Co_{0.2}Cu_{0.2}Mg_{0.2}Ni_{0.2}Zn_{0.2})O$ with rock-salt structure was first reported by Rost et al.[20], and used as an anode material for LIBs in 2018 [21]. Compared to conventional TMOs, the configurational entropy stability of HEO lattices and the doping of inactive materials (MgO) lead to LIBs with superior performance. On the other hand, $(MnFeCoNiCr)_3O_4$ has been shown to exhibit a reversible capacity of 500 mA h g^{-1} at 2000 mA

* Corresponding author.
E-mail address: hytuan@che.nthu.edu.tw (H.-Y. Tuan).

https://doi.org/10.1016/j.cej.2022.137924
Received 7 April 2022; Received in revised form 14 June 2022; Accepted 2 July 2022
Available online 5 July 2022

$g^{-1}$and 90% capacity retention after 200 cycles at a current density of 500 mA g^{-1} by Nguyen et al.[22] Although HEOs outperformed TMOs in LIBs, there is still room for improvement in rate performance and cycling stability, mainly due to their poor electrical conductivity and structural stability limiting the electrochemical performance. [23,24].

Interface engineering modifies the surface of active materials through chemical modification, thereby enhancing the electrochemical performance of electrode materials and improving the interaction between materials and electrolytes [25,26]. In LIBs, the reduction of the particle sizes of active materials decreases the diffusion resistance of lithium ions, increases the contact interface, and promotes the penetration of Li^+ between the material and electrolyte. However, the high specific surface area of nanoparticles leads to particle aggregation and obvious irreversible reactions. Therefore, coating electrochemically stable compounds (oxides, fluorides, carbons and polymers) has been used to modify the interfacial reactivity of materials [27,28,29]. Conductive polymer is one of the most commonly surface modification materials in interface engineering, which is a kind of highly π-conjugated polymer chain, easy to synthesize, strong acid/base doping ability, high conductivity, optical activity and environmental stability. Taking polyaniline (PANI) as an example, emeraldine is the most stable and conductive in PANI and can be doped by proton acids (HCl, Phytic acid) apart from conventional redox doping [30]. PANI has the functions of stabilizing the structure, improving conductivity, and promoting the lithium ionic conductivity. When applied to anode materials including TMOs (NiO, TiO_2, SnO_2 and Fe_2O_3), PANI has been shown to be effective in improving material stability and conductivity [31,32,33,34] and metal sulfides (SnS_2, MoS_2) [35,36] For example, flexible protective layer of PANI on SnO surface greatly improves the cycling performance and rate capability in LIB [37].

As shown in Scheme 1, when the HEO anode reacts with Li^+ leading to partial structural rupture, the exposure of the SEI increases the contact area between the electrolyte and the material, thereby increasing the production of non-conductive species (LiF) on the SEI during cycling and hindering the transport of Li^+. In addition, the reaction of the electrolyte $LiPF_6$ with traces of water during cycles generate HF, which may dissolve high-entropy oxides [38 39], resulting in the inevitable decay of capacity. Here, we utilize PANI surface polymerization to modify the interfacial properties of HEO to improve their electrochemical performance when used as LIB anodes. Surface PANI coating effectively blocks the contact between electrolyte and material which inhibit the side reaction. Moreover, flexibility PANI buffering volume expansion and trapping refined pieces to lessen capacity decay. The PANI-coated HEO, whose coating thickness only needs a few nanometers and a low ratio (~6%), have enhanced composite structure stability and electrical conductivity, and can also suppress the overgrowth of SEI, as well as the absorption of HF in the electrolyte by proton doping. Comprehensive performance of capacity at 0.1 A g^{-1}, capacity at 1 A g^{-1}, initial Coulomb efficiency, maximum current density and cycles number, PANI-coated HEO shows excellent performance. Moreover, we assembled full cell of HEO-MP //NCM with capacity retention after 120 cycles and the pouch type full cell with the capacity of 10 mAh successfully applied to light up 140 LEDs. This result provides new insights into the positive role of interfacial engineering for HEO LIB electrodes to enhance their electrochemical performance.

2. Experimental section

2.1. Synthesis of HEO

The HEO was synthesized by hydrothermal method and heat treatment. First, the precursor solution was prepared by dissolving 1.5 mmol $Co(NO_3)_2{\cdot}6H_2O$, $Mg(NO_3)_2{\cdot}6H_2O$, $Cu(NO_3)_2{\cdot}2.5H_2O$, $Zn(NO_3)_2{\cdot}6H_2O$ and $Ni(NO_3)_2{\cdot}6H_2O$ in 40 ml DI water, followed by the addition of 0.25 g of CTAB. After stirring for few minute 1.0 g urea was added to the solution. The resulting solution was transferred to Teflon lined autoclave and heated to 140 °C for 5 h. The green powder was collected by centrifugation and washing with ethanol and DI water three times. After hydrothermal treatment, HEO was obtained after calcination in air at 800 °C for 2 h with a heating rate of 10 °C min^{-1}. The as-prepared HEO power were milled into nanoparticles with steel balls in isopropyl alcohol for 72 h to HEO-M.

2.2. Synthesis of HEO-MP

In a typical procedure, 70 mg HEO-M was dispersed in 5 ml DI water by ultrasound. Then, 20 μl aniline monomer and 40 μl phytic acid solution (50%) were added into the mixture solution under ultrasound. Final, a solution of 30 mg of ammonium persulfate, $(NH_4)_2S_2O_8$ (APS), in 1 ml DI water were added into the mixture solution. This reaction was conducted for 12 h in refrigerator. The product was collected by centrifugation and washing with ethanol and DI water three times. For comparison, HEO-G and HEO-CNT were synthesized through coating graphite and CNT with HEO-M by ball milling, respectively.

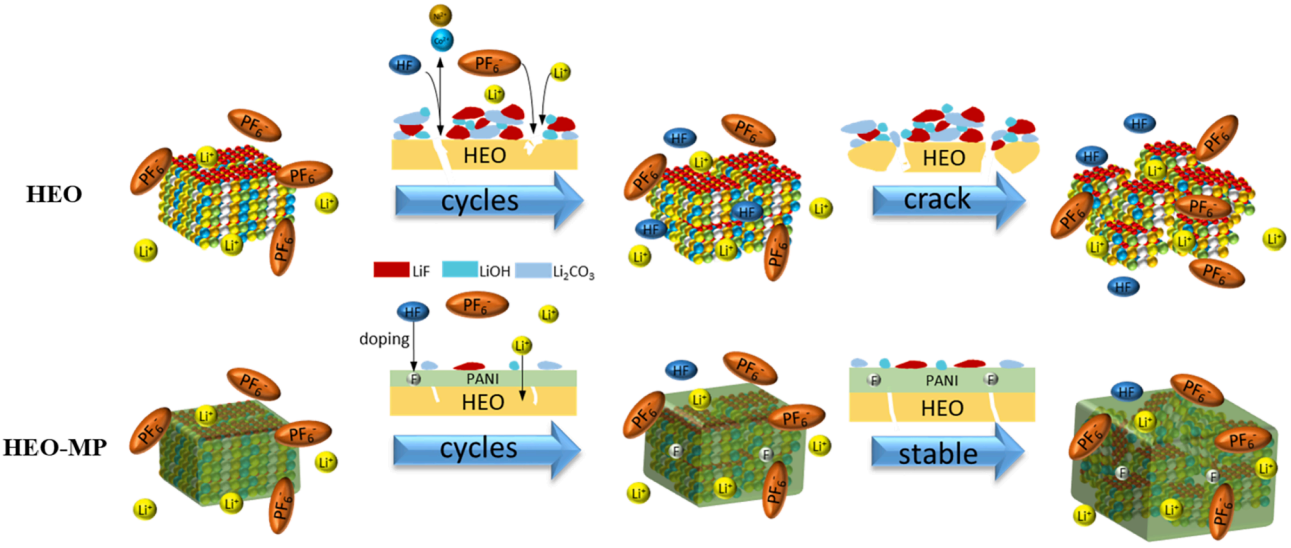

Scheme 1. Schematic illustrations of PANI interface engineering inhibiting the side reaction and trapping refined HEO during cycles.

2.3. Material characterization

The X-ray diffractometer (XRD, D8 advance eco (Bruker)) data were obtained with Cu-Kα radiation. The morphologies were acquired by scanning electron microscopy (SEM) (Hitachi SU8010) equipped with energy-dispersive X-ray spectroscopy (EDS) detector. Transmission electron microscopy (TEM) (JEOL, JEM-ARM200FTH, services provided by NTHU and JEOL, JEM-2100F services provided by NTU) with an accelerating voltage of 200 kV for investigating further structure analysis including morphology, HRTEM, EDS, and SAED. The X-ray photoelectron spectroscopy (XPS) characteristic peaks were conducted with ULVAC-PHI Quantera II. All the spectra obtained from XPS analysis were first calibrated by referencing binding energy of C 1 s (284.8 eV), followed by the curve fitting using the software of XPSPEAK VER. 4.1. Thermogravimetric analysis (TGA) was conducted in N_2 using a thermogravimetric analyzer (TA, Q50) from 50 ∘C to 800 ∘C with a heating rate of 10 °C min^{-1}. TOF-SIMS data were collected on a TOF-SIMS V spectrometer (ION-TOF GmbH). A pulsed 30 keV Bi_1^+ (20 ns) ion beam was applied for depth profiling. 1 keV Cs^+ (negative mode) ion beam was used for the sputtering with a typical area of 260 μm × 260 μm. A typical area for depth profiling analysis was 100 μm × 100 μm.

2.4. Electrochemical characterization

The working electrode, HEO, HEO-M and HEO-MP were prepared by mixing 70% active material, 20% Super-P, and 10% CMC binder by weight in deionized water to form a slurry coated on copper foil, followed by vacuum-drying. The average mass loading of the active material was ~ 1.0 mg cm^{-2}. The electrochemical properties of the as-prepared electrodes were evaluated by assembling CR 2032-type coin

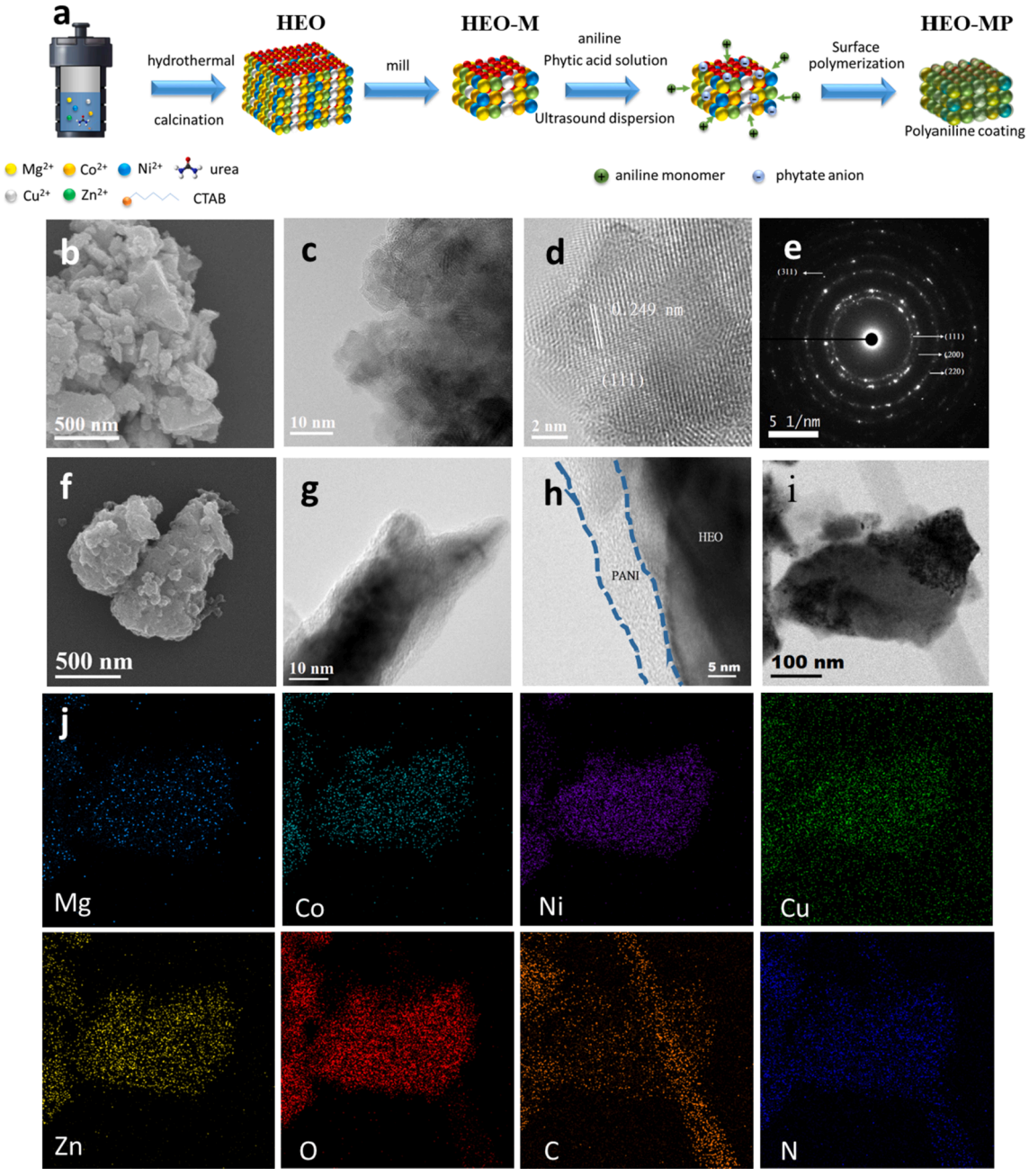

Fig. 1. (a) Schematic illustration for the preparation of HEO-MP. (b) SEM, (c, d) TEM and (e) SAED images of HEO-M; (f) SEM and (g, h) TEM images of HEO-MP; (i, j) TEM image and corresponding element mapping images of HEO-MP.

cells in the argon-filled glovebox. For half-cell, Li metal foil was utilized as the counter/reference electrode, and microporous polyethylene separator soaked in electrolyte. 1 M $LiPF_6$ (in EC:DEC:FEC = 5:5:1) as the electrolyte. For full-cell, the NCM cathode was prepared by mixing 80% active material, 10% Super-P, and 10% PVDF binder by weight in NMP to form a slurry coated on aluminum foil. The areal loadings in full cell were around ~ 4 mg_{NCM} cm^{-2} and ~ 1 $mg_{HEO\text{-}MP}$ cm^{-2}. 1 M $LiPF_6$ (in EC:DMC = 1:1) as the electrolyte. The galvanostatic charge/discharge tests were conducted within the voltage range of 0.01–3.0 V. Cyclic voltammetry (CV) tests and electrochemical impedance spectroscopy (EIS) tests were conducted on a Biologic VMP3 electrochemistry workstation.

3. Results and discussion

The overall synthesis process for HEO-MP is as illustrated in Fig. 1a. HEO was obtained by a hydrothermal process, in which carbonate and ammonium (obtained from the hydrolysis of urea) reacted with metal ions to produce precipitates containing metal hydroxycarbonates and hydrocarbon, hydroxides, etc [40]. HEO was obtained after calcination of the precipitate precursors in air at 800 °C. Then, micrometer-sized HEO (HEO-M) was produced by high-energy ball milling HEO. Upon subsequent, the HEO-M was uniformly dispersed into the solution by ultrasonic vibration which adsorbed the phytic acid protonated aniline monomer [41,42]. The surface polymerization was initiated by the oxidant ammonium persulfate, and the particles were coated with PANI to synthesize HEO-MP. The diffraction peaks at 36.8°, 42.8°, 61.9°, 74.2° and 78.0° can be indexed to (111), (200), (220), (311) and (222) planes of rocksalt structure HEO [43]. In addition, the signal intensity of XRD decreased significantly after ball milling, indicating that the lattice structure was destroyed which lead to decrease of the reflected signal of X-ray after ball milling in Fig. S1. The ICP-MS shows that the elements of Mg, Co, Ni, Cu and Zn in HEO are 5.39, 20.86, 22.11, 28.06 and 23.59 in atomic% which confirm the chemical formula of HEO is $(Mg_{0.05}Co_{0.21}Ni_{0.22}Cu_{0.28}Zn_{0.24})O$. The relatively high solubility of Mg precipitate in hydrothermal process, which decrease the proportion of Mg in HEO. However, the configurational entropy is 1.51R which belongs to high entropy materials. The morphology of HEO-M and HEO-MP are primarily investigated by scanning electron microscopy (SEM) in Fig. 1b, f. HEO-M exhibits particle sizes of around 1 μm after ball milling in Fig. 1b. After coating with PANI, the particle surface is obviously rough as shown in Fig. 1f. The transmission electron microscopy (TEM) image and selected area electron diffraction (SAED) pattern reveal that HEO-M still has a polycrystalline structure (Fig. 1c). The polycrystalline diffraction rings of SAED pattern (Fig. 1e) presents the microstructural characteristics of a typical FCC structure, where the (111), (200), (220) and (311) diffraction planes with *d* spacings of 0.249, 0.211, 0.152 and 0.126 nm, respectively. The TEM images of HEO-M and HEO-MP (Fig. 1c, g) clearly show the PANI coating. Furthermore, Fig. 1h shows that the as-obtained of PANI is about 5 nm thick and uniform distribution that proves the polymerization of PANI on the surface of HEO-MP. To study the elemental composition of HEO-MP, the HRTEM-EDS spectra and element mappings of HEO-MP are shown in Fig. 1i, j. The elements of Mg, Co, Ni, Cu, Zn, and O are homogeneously distributed within the region of a single particle. In addition, the signals of C and N on the surface of HEO indicate that the surface is indeed covered by PANI.

Detailed characteristic information of PANI coating on HEO is further investigated by Fourier-transform infrared spectroscopy (FTIR), Raman and TGA. The FTIR spectra of PANI, HEO-M and HEO-MP are displayed in Fig. 2a. The characteristic peaks of PANI at 1543 cm^{-1} and 1457 cm^{-1} are attributed to N = Q = N stretching vibration and C = C stretching vibration [44]. Compared with the FTIR spectrum of HEO-M and HEO-MP, HEO-MP contains the characteristic peaks of PANI at 1457 cm^{-1} and 1543 cm^{-1}. Fig. 2b shows the Raman spectrum of PANI, HEO-M and HEO-MP. There are distinct characteristic peaks at

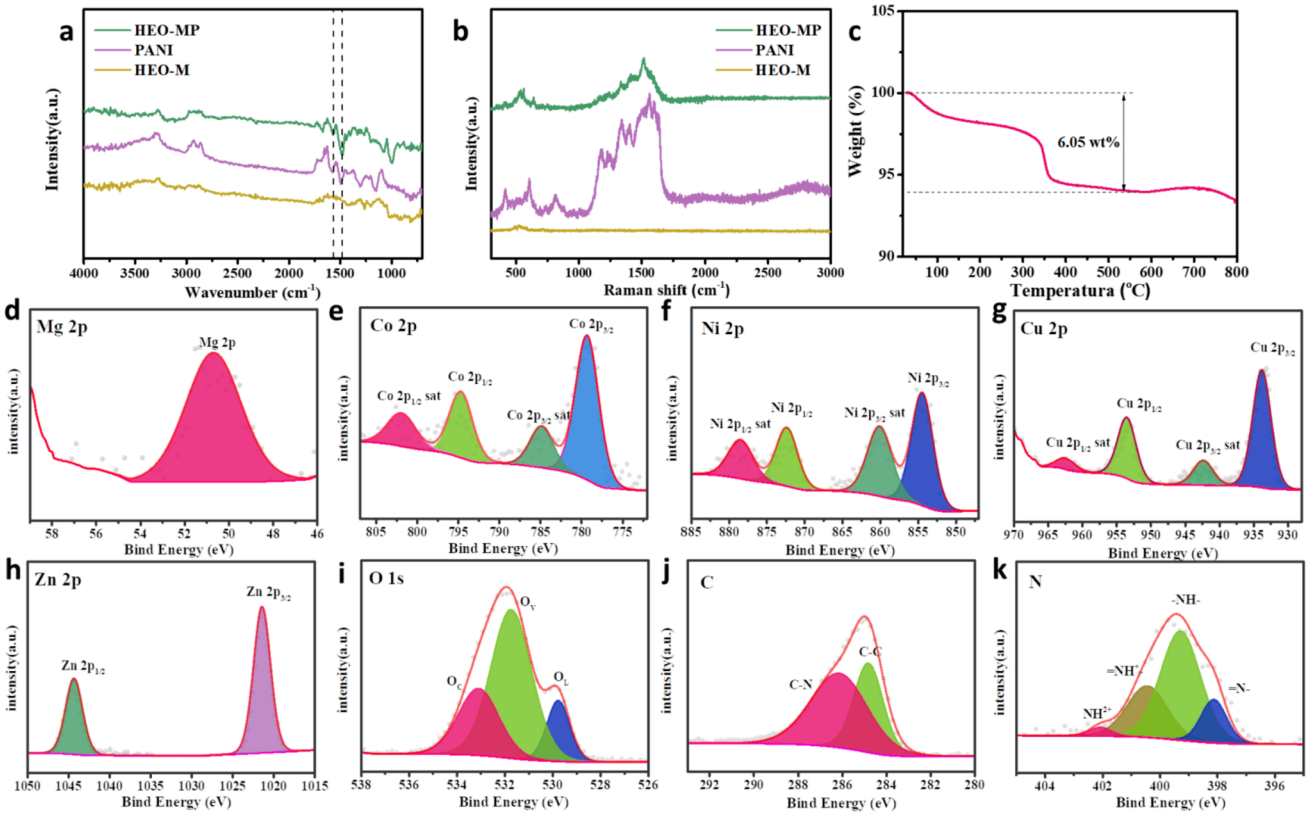

Fig. 2. (a) FTIR and (b) Raman spectra of HEO-MP, PANI and HEO-M; (c) TGA and (d-k) High-resolution XPS of the element (d) Mg, (e) Co, (f) Ni, (g) Cu, (h) Zn, (i) O, (j) C and (k) N of HEO-MP.

1000–1700 cm^{-1} for PANI, including C–H bending vibration of benzene ring at 1165 cm^{-1} and N stretching of C = C quinoid ring at 1494 cm^{-1} and C–C stretch with benzene ring at 1595 cm^{-1} [31]. HEO-MP has obvious characteristic peak of PANI compared with HEO-M, which indicates the flexible PANI polymer successfully covers on the surface of HEO. TGA is used to determine the proportion of PANI on HEO-MP in Fig. 2c. Two distinctive degradation steps of PANI are observed. First, the PANI is gradually carbonized before 300 °C. Second, the sharp drop in weight at 380 °C indicates that the carbonized PANI was burned into carbon dioxide. Therefore, the original fraction of PANI in the HEO-MP composite was measured to be 6.05%, and the proportion of HEO was 93.95%. The XPS measurement is performed to study the surface chemistry of HEO-MP in Fig. 2d-k. In the Mg 2p XPS spectrum (Fig. 2d), the peak at 50.7 eV is typical of Mg-O bonds with Mg^{2+}. Four peaks located at 781.2, 786.0, 797.0, and 803.3 eV in the Co 2p spectrum (Fig. 2e) is a typical Co^{2+} oxidation state indexed to Co $2p_{3/2}$, a satellite peak, Co $2p_{1/2}$, and a satellite peak, respectively. The Ni 2p spectrum is shown in Fig. 2f, the peaks at 856.3 eV (Ni $2p_{3/2}$) and 874.3 eV (Ni $2p_{1/2}$) are corresponding to Ni^{2+}. Moreover, two clear satellite peaks at 862.0 eV and 880.3 eV can also be observed. The Cu 2p spectrum is shown in Fig. 2g, the Cu $2p_{3/2}$ and Cu $2p_{1/2}$ peaks are located at 933.7 eV and 953.4 eV. In addition, two clear satellite peaks at 942.3 eV and 962.4 eV can be observed. In the Zn 2p XPS spectrum (Fig. 2h), the typical Zn^{2+} peaks of Zn $2p_{3/2}$ and Zn $2p_{1/2}$ are located at 1022.8 and 1045.7 eV. The O1s spectra (Fig. 2i) shows lattice oxygen (O_L) for metal oxides, oxygen vacancy (O_V) for oxygen-containing functional groups (PO, OH) in phytic acid-doped PANI, and chemisorbed oxygen (O_C) components at 529.7, 531.8, and 533.1 eV, respectively. In the C XPS spectrum (Fig. 2j), the respective peaks of C–C and C-N bonds at 284.8 eV and 286.1 eV, are derived from noise interference or PANI coating. According to the N XPS spectrum (Fig. 2k), the peaks located at 398.0 eV, 399.2 eV, 400.3 eV and 402.0 eV represent the quinidine phenyl structure (=N-), benzene structure (–NH-) and ammonium salt structure (=NH^{+}-, NH^{2+}) [45], the existence of PANI is also proved in XPS.

The half-cell electrochemical performance in HEO-MP is summarized in Fig. 3. The first three cyclic voltammogram (CV) curves of the HEO-MP composite electrode between 0.01 and 3.0 V at a scan rate of 0.1 mV s^{-1} is shown in Fig. 3a. In the first discharge cycle, the irreversible peak is observed at 0.62 V, which is ascribed to the electrolyte decomposition and SEI formation. The reduction peak at 1.01 V corresponds to the lithiation reactions which lithium ions reacts with HEO-MP and product Li_2O and metal. After the discharge cycle, two oxidation peaks are observed at 1.78 and 2.11 V, which are associated with delithiation reactions that metal reacts with Li_2O to produce metal oxide and release lithium ions. Furthermore, the CV curves obtained after the first scan nearly overlap, indicating that the reactions are excellent reversibility. Fig. 3b shows voltage profiles of HEO-MP at a current density of 0.1 A g^{-1} between 0.01 and 3.00 V, where HEO-MP electrode delivers an initial discharge and charge capacities of 1107.9 and 807.8 mA h g^{-1} with 72.9% ICE. The discharge/charge curves are consistent with the CV results, the plateau is mainly around 1.5 ~ 2.1 V during charging, and the plateau is mainly around 1.5 ~ 0.8 V during discharging. Fig. 3c shows the reversible capacities of HEO, HEO-M, and HEO-MP at 500 mA g^{-1}. Both the capacities of HEO-M and HEO-MP are higher than HEO because of the smaller particle size after activity by ball milling. In addition, the capacity of HEO-M is slightly higher than HEO-MP before 15 cycles; however, the capacity still decays rapidly. After 100 cycles, HEO, HEO-M and HEO-MP electrodes deliver the reversible capacities of 442.1, 338.9 and 822.7 mA h g^{-1}, respectively. Conversely, the HEO-MP maintains a high capacity in the following cycles. After 100 cycles, HEO,

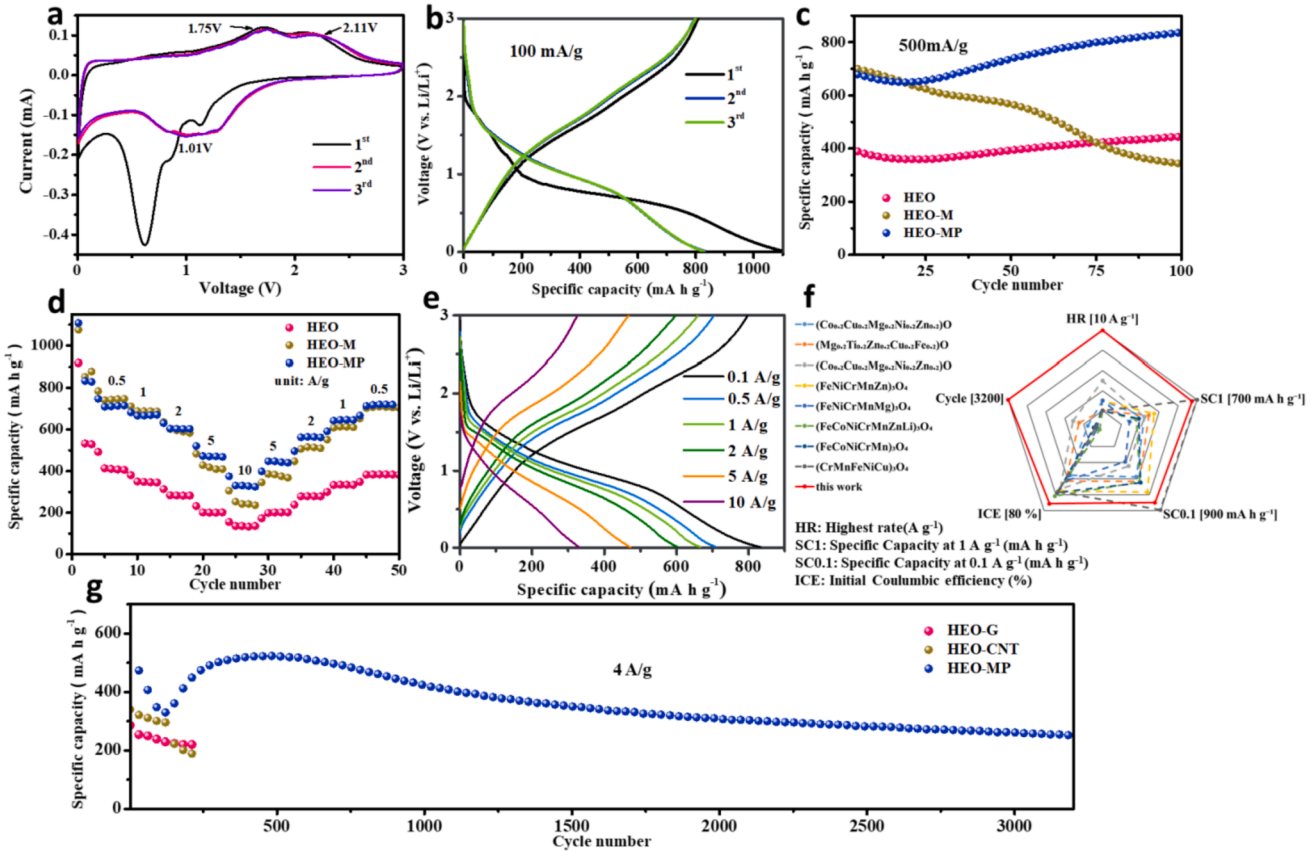

Fig. 3. (a) The CV curves of HEO-MP at 0.1 mV s^{-1}; (b) The charge–discharge curves of HEO-MP at 100 mA g^{-1}; (c) The cycle performance for the HEO, HEO-M and HEO-MP; (d) The rate capability of HEO, HEO-M and HEO-MP; (e) The charge–discharge plots of HEO-MP at different current densities; (f) Comparison of the electrochemical performance of recently published HEO electrode; (g) The long-term cycle stability of HEO-G, HEO-CNT and HEO-MP at 4.0 A g^{-1}.

HEO-M and HEO-MP electrodes deliver the reversible capacities of 442.1, 338.9 and 822.7 mA h g^{-1}, respectively. The rate performances of three samples are investigated in Fig. 3d. HEO-MP displays high charge capacities of 705.2, 663.0, 598.4, 466.6 and 325.0 mA h g^{-1} at 0.5, 1, 2, 5 and 10 A g^{-1} in Fig. 3e, respectively. HEO-M displays charge capacities of 731.1, 680.0, 582.3, 412.5 and 241.6 mA h g^{-1} at 0.5, 1, 2, 5 and 10 A g^{-1}, respectively. These results suggest that HEO-MP has an excellent rate performance due to the stable structure and enhancing conductivity by PANI, especially at a high current density of 10 A g^{-1}. There is no obvious capacity decay at the current density of 0.5 A g^{-1}. HEO displays charge capacities of 409.4, 346.4, 281.6, 198.6 and 133.3 mA h g^{-1} at 0.5, 1, 2, 5 and 10 A g^{-1}, which is significantly lower than HEO-M and HEO-MP. Fig. 3f shows a comparison of the electrochemical performance of the recent published HEO electrode with this work. The radar plot shows initial Coulombic efficiency (ICE), specific capacity at low rate (SC0.1), specific capacity at high rate (SC1), highest rate (HR), and number of cycles. We compared eight HEO electrode materials, including rock-salt HEO $(Mg_{0.2}Co_{0.2}Ni_{0.2}Cu_{0.2}Zn_{0.2})O$ and spinel HEO $(Mg_{0.2}Ti_{0.2}Zn_{0.2}Cu_{0.2}Fe_{0.2})_3O_4$, $(FeNiCrMnZn)_3O_4$, $(FeNiCrMnMg)_3O_4$, $(FeCoNiCrMnZnLi)_3O_4$ and $(FeCoNiCrMn)_3O_4$ [21,46,47,48,49,50,51]. This work covers the largest area, which means that the excellent electrochemical performance of HEO-MP. It demonstrates the best performance in terms of the highest rate (10 A g^{-1}) and cycles (3200) performance in HEO electrode materials. Fig. 3g shows the long-term cycle stability of HEO-G, HEO-CNT and HEO-MP at high current density of 4.0 A g^{-1}. The capacity of HEO-G and HEO-CNT continuously decay. It indicates that the coating of carbon can't improve the stability of HEO in high rate. In contrast, HEO-MP ameliorates the stability with PANI coating. After 3200 cycles, a high capacity of 261 mA h g^{-1} is retained.

To clarify the capacitive and diffusion-controlled effects of the HEO-MP, the Li ion storage kinetics was analyzed on the basis of the CV measurements. Fig. 4a shows the CV curves at various scan rates from 0.2 to 1 mV s^{-1}. The CV profile exhibits distinct redox peaks with increasing peak current (i) as scan rate (v: 0.2–1 mV s^{-1}) increases, which can be shown as $i = av^b$. The a and b are empirical parameters. The b-value is closer to 0.5, the system is controlled by diffusion, while the b-value is closer to 1, the system is pseudocapacitive-controlled process. A plot of log(i)-log(v) can yield parameter a and b. The b-value of peak 1 and peak 2 can be determined to be 0.75 and 0.86 (Fig. 4b). These values indicate the mixed capacitive- and diffusion-controlled electrode kinetics. To further separate the contribution, the total current response (i) at a fixed potential (V) can be separated into two mechanisms of capacitive ($k_1\nu$) and diffusion-controlled processes ($k_2\nu^{1/2}$) according to the following equation: $i = (k_1\nu) + (k_2\nu^{1/2})$. By plotting i (V)/$v^{1/2}$ versus $v^{1/2}$ at a fixed potential, the values of k_1 and k_2 can be calculated and the capacitive current $i_c(V) = k_1\nu$ could be distinguished from the total measured current with the value of k_2. Fig. 4c shows that nearly 73.8% of the total charge storage originates from capacitive contribution at a scan rate of 0.6 mV s^{-1}. Fig. 4d shows that the capacitive contribution is 66.4%, 70.2%, 73.8%, 78.3% and 82.5% at scan rates of 0.2, 0.4, 0.6, 0.8 and 1.0 mV s^{-1}, respectively. The large capacitive contribution is considered to be from the electrical double-layer capacitance and Faradic pseudocapacitance created by Li^+ adsorption/desorption. In contrast, the capacitive contribution of HEO-M is 54.2%, 59.9%, 64.8%, 69.5% and 72.4% at scan rates of 0.2, 0.4, 0.6, 0.8 and 1.0 mV s^{-1}, respectively. The capacitance contribution of HEO-MP is higher than HEO-M because the PANI layer enhances electron transport in conversion reaction [52]. The pseudocapacitance of HEO at high current densities is faster due to the high conductivity of PANI. At a scan rate of 0.6 mV s^{-1}, the capacitance contribution of HEO-MP is 73.8% which is higher than HEO-M, further demonstrating the

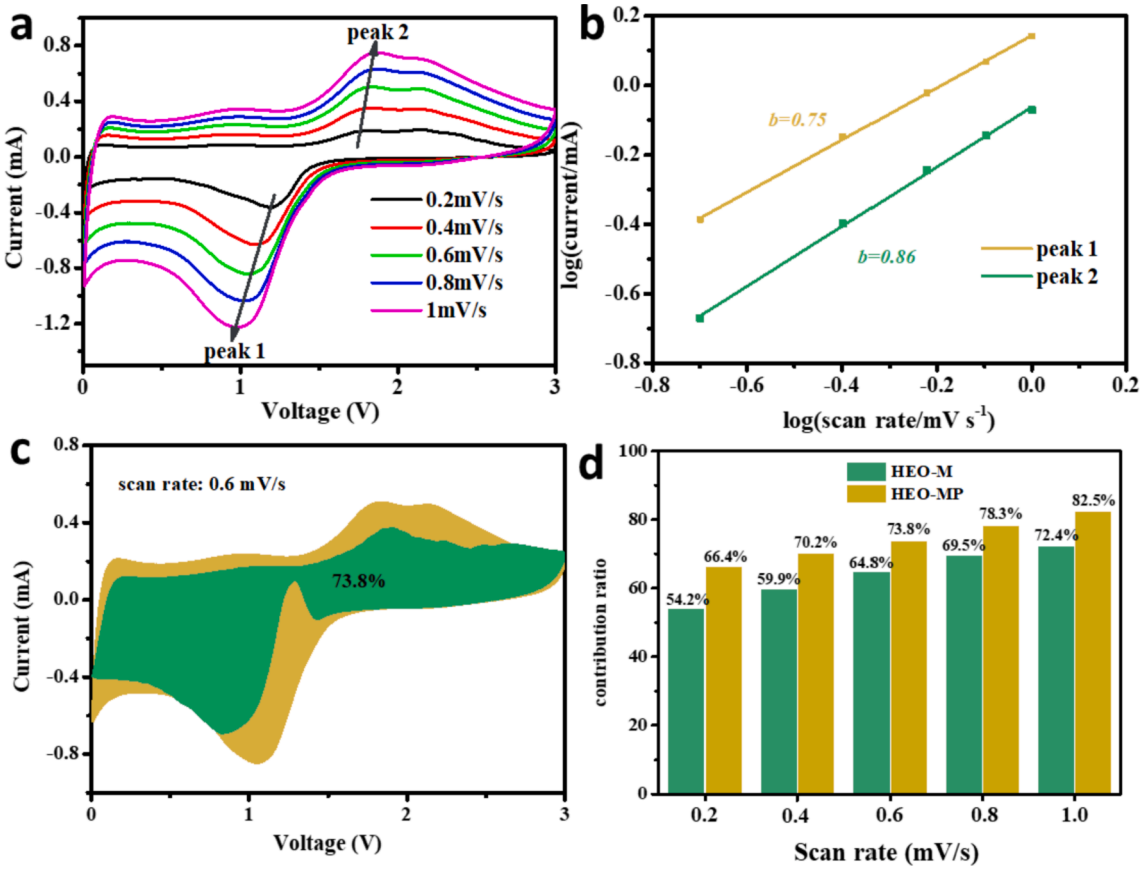

Fig. 4. (a) CV cures at different scan rates from 0.2 to 1.0 mV s^{-1}; (b) the linear relationship of log(I_p) vs log(v); (c) the CV profiles displaying capacitive contribution at 0.6 mV s^{-1} of HEO-MP; (d) The ratio of capacitance contribution at different scan rates of HEO-M and HEO-MP.

remarkable effect of PANI on high rate performance.

To further investigate the reaction mechanism, in situ XRD analysis and SAED are conducted to observe the reaction mechanism. Fig. S9a shows the obtained XRD patterns during the initial three cycles. The diffraction peaks (1 1 1) and (2 0 0) located at 36.8° and 42.8° gradually diminished and the intensity nearly disappears when the lithiation potential approached the terminal value of 0.01 V, indicating the local structure rearrangement and an amorphous structure are obtained after discharging [21]. When the conversion reaction $M_xO_y + 2yLi \leftrightarrow xM + yLi_2O$ product small crystallites during the discharge process, the signal lower than the detection threshold of XRD [3]. The SAED in Fig. S9c shows the diffraction rings belong to the (1 1 1) of Li_2O which confirm the conversion reaction in HEO. We conducted in situ electrochemical impedance spectroscopy (EIS) kinetic measurements to explore the electrochemical kinetics during the charge/discharge process. Starting from a potential of 2.9 V (open-circuit voltage (OCV)), we conducted the discharge and charge processes between 0.01 and 3.0 V at a current density of 0.1 A g^{-1}. Fig. 5a, b present the Nyquist plots of HEO-MP during the in situ EIS analysis in initial cycle. As the electrode discharged from OCV to 1.5 V, the formation of the SEI layer slightly increases the resistance. When discharge to 0.5 V, the lithium ions react with HEO, Li_2O and metal (Ni, Cu, etc.) are gradually produced in the structure, which gradually decrease the resistance. However, when discharging to 0.01 V, the resistance slightly increased, we presumed that Li_2O was complete generated to increase the resistance. When charged to 3.0 V, metal (Ni, Cu, etc.) react with Li_2O to produce metal

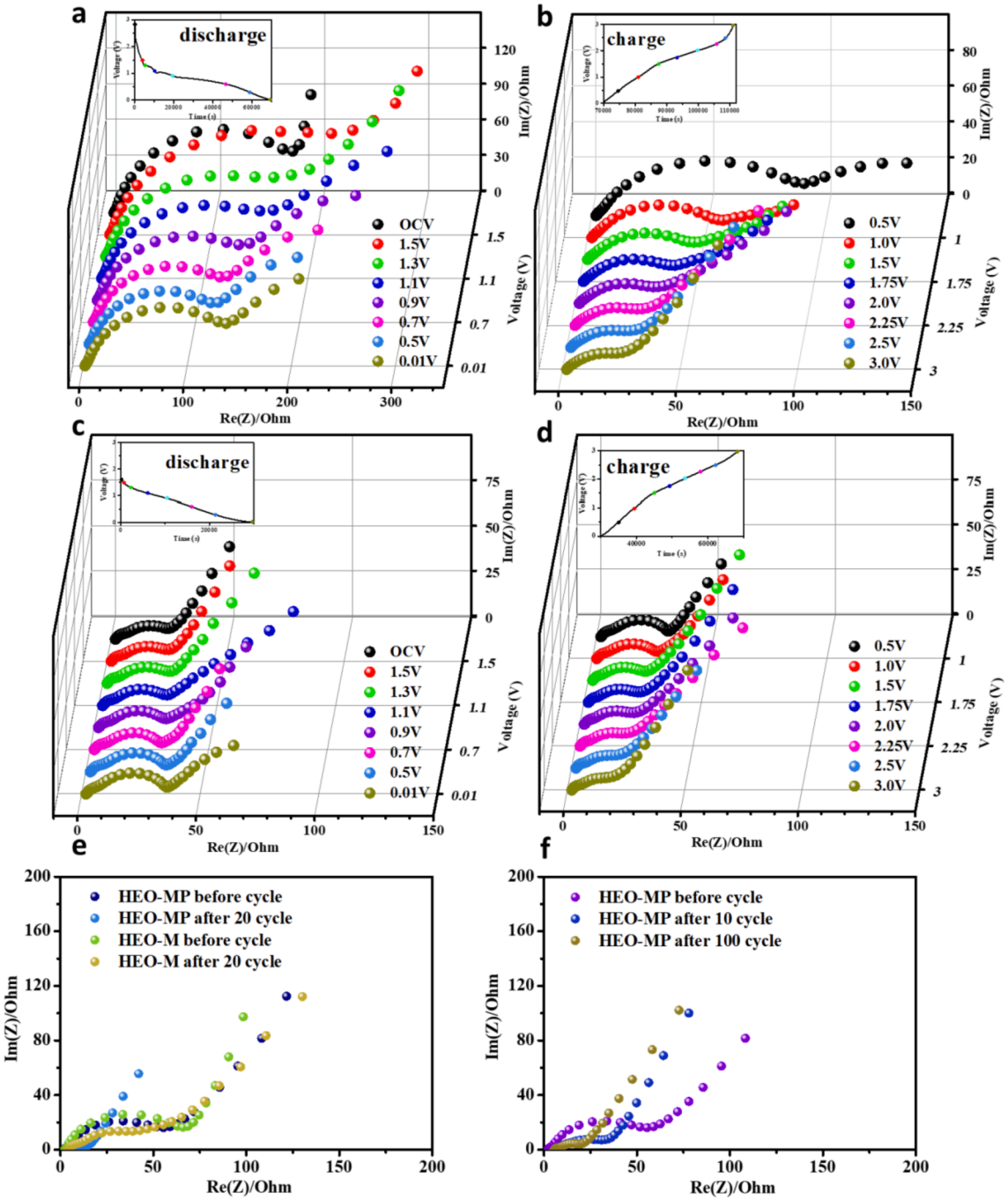

Fig. 5. In situ EIS of HEO-MP for the (a, b)1st cycle and (c, d) 20th cycle; (e) EIS of HEO-M and HEO-MP before and after 20 cycles; (f) EIS of HEO-MP before, 10th and 100th cycle.

oxide (NiO, CuO, etc.) which decrease charge transfer resistances. Fig. 5c, d present the Nyquist plots of HEO-MP during the in situ EIS analysis in the 20th cycle. When discharged to 0.5 V, there is no significant change in resistance, which can be attributed to the formation of stable SEI layer and activation of the electrode material. Next, the resistance increases slightly during discharge to 0.01 V, which may be attributed to the product of Li_2O. When charged to 3.0 V, there is no significant change in resistance except a slight decrease in resistance initially (disappearance of Li_2O). This is attributed to the stability of conversion reaction and SEI in HEO-MP. Fig. 5e shows the EIS of HEO-M and HEO-MP before and after 20 cycles. HEO-M shows higher charge transfer resistance (R_{ct}) than HEO-MP and the R_{ct} of HEO-MP decreases significantly after 20 cycles. We speculate that HEO-MP has better conductivity due to the coating of PANI. Moreover, it can effectively prevent HEO contact with electrolyte to reduce the formation of non-conductive impurities. In contrast, HEO-M generates more non-conductive impurities (LiF) because of the SEI cracking during cycles. Therefore, the resistance of SEI on the surface of HEO-MP is much less than HEO-M. Fig. 5f shows the EIS of HEO-MP anode in different cycles. The R_{ct} of HEO-MP decreases during cycles because the refined materials increase the ion transport channel and PANI inhibit the production of non-conductive impurities (LiF). Consequently, these results demonstrate the superior kinetics of HEO-MP.

We investigated the TEM and SEM of the cycled electrode to further explore the phenomenon of PANI protective materials. The images of HEO-MP anode before cycle, 20th cycle and 50th cycle are displayed in Fig. 6. It can be observed that the material is clearly bulky and covered by PANI in Fig. 6d. The inner material appears granular structure in 20th cycle (Fig. 6e), and ~ 10 nm nanoparticles are generated within the PANI layer in 50th cycle (Fig. 6f) due to the volume change in the conversion reaction. On the other hand, PANI layer effectively maintains the structure in Fig. 6a-c where the morphology of material only slightly changes. In contrast, HEO-M is partially fractured during cycles (Fig. S10). Consequently, the uniform PANI coating effectively buffer the volume expansion and trapping refined HEO pieces during lithiation-delithiation process which avoids SEI cracking and prevents the generation of non-conductive impurities.

Time-of-flight secondary ion mass spectrometry (TOF-SIMS) is performed to probe the surface chemistry of HEO-MP and HEO-M. The N-containing secondary ion fragments (CN^-) are attributed to PANI, Co^- and Ni^- confirming the presence of HEO. The uncycled HEO-MP shows relatively weak signals for Co^- and Ni^- (the presence of HEO) and strong signals of CN^- (the presence of PANI) than HEO-M in Fig. S11, which shows PANI coating. After cycles, the signals stand for the key components of SEI ($LiOH^-$, LiF^-, and $LiCO_3^-$) are intensified (Fig. S12) which indicates the generation of SEI. No significant difference in Co^- and Ni^- signals in HEO-MP and HEO-M due to the shading of SEI. To explore the SEI evolution upon cycling, we conducted TOF-SIMS depth analysis from HEO-M and HEO-MP electrodes with different cycles (Fig. 7). In the HEO-M electrodes (Fig. 7a, b), LiF^- obviously penetrates into the electrode in the first cycle and uniformly distributes inside the electrode in 50th cycle. In contrast, LiF^- mainly existed within the 300 s of sputtering time in the first cycle of HEO-MP and did not significantly penetrates into the interior which remain on the surface in 50th cycle. The electrolyte-swollen PANI enables doping of the polymer matrix with Li^+ and absorbs corrosive hydrogen fluoride which protects and regulates the stable SEI [53]. Therefore, the electrode of HEO-M is easily penetrated and hinder the charge transport, which affect the battery performance.

The outstanding Li^+ storage properties of HEO-MP are associated with uniform PANI coating, which overcome the disadvantages of HEO include poor conductivity and the volume expansion. Conductive PANI with the conjugated π electron system enhances the conductivity of HEO by interface coating. Furthermore, flexible PANI effectively traps the refined active materials during cycles. Ex situ TEM (Fig. 6) confirm that the nano size HEO is encapsulated in the PANI. Therefore, HEO-MP anode exhibits excellent performance for 3200 cycles at a high current density of 4 A g^{-1}. PANI also improves the interfacial reaction between the material and electrolyte. The electrolyte ($LiPF_6$) reacts with trace water during charge and discharge as follows:

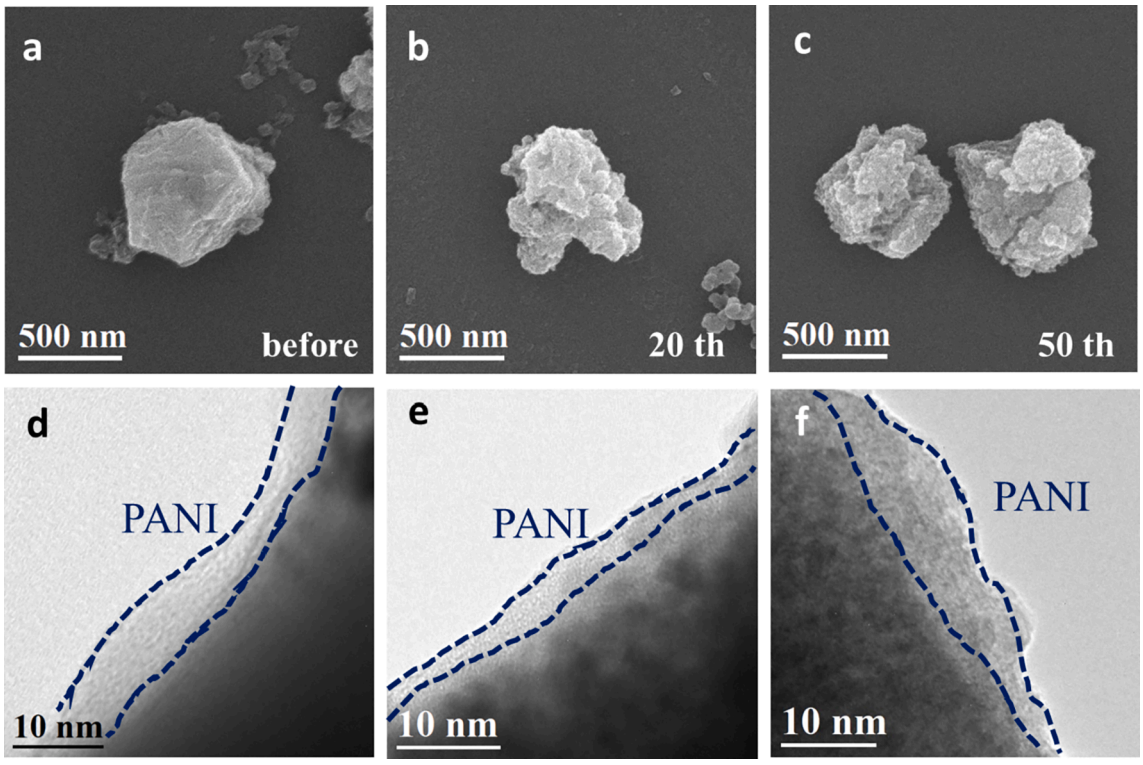

Fig. 6. SEM images of HEO-MP anode (a) before cycle, (b) 20th cycle and (c) 50th cycle; TEM images of HEO-MP anode (d) before cycle, (e) 20th cycle and (f) 50th cycle;

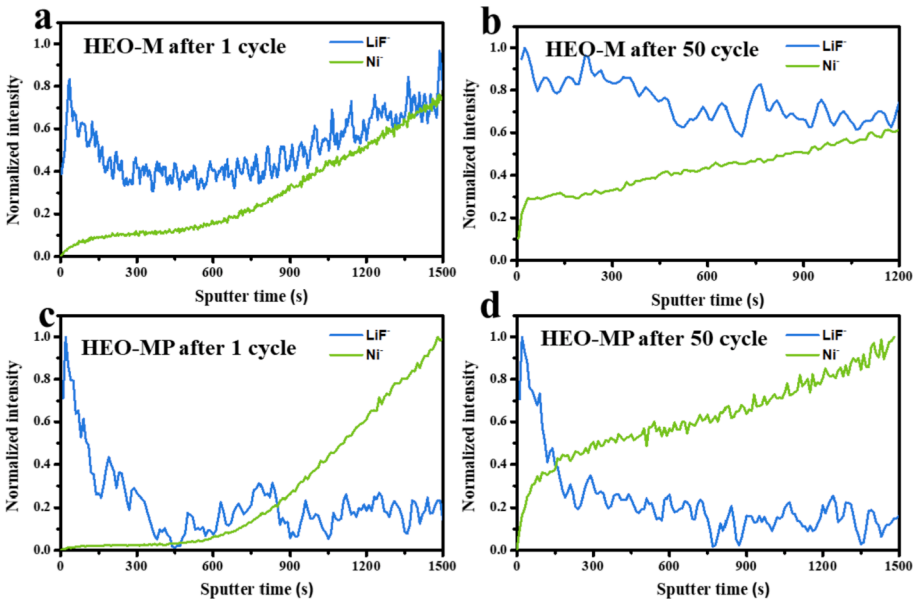

Fig. 7. Normalized negative ion depth distributions from the HEO-M anode after (a) the first cycle and after (b) the 50th cycle; the HEO-MP anode after (c) the first cycle and after (d) the 50th cycle.

$LiPF_6 + H_2O \leftrightarrow LiF\downarrow + POF_3 + 2HF$

LiF is a non-conductive impurity. When it is excessively accumulated in the SEI, it hinders the transport of Li^+ and increase the resistance. In addition, HF dissolves transition metals in HEO (Ni^{2+}, Co^{2+} etc.), and reacts with Li_2O:

$Li_2O + 2HF \rightarrow 2LiF + 2H_2O$

Finally, the material is partially cracked (Fig. S10). Furthermore, the rupture of the SEI increases the contact area between the electrolyte and material, which leads to unstable SEI and the side product of HF. PANI has the following merits to improve the properties. First, the thin layer of PANI swollen with electrolyte blocks the contact between electrolyte and material to prevent continuous accumulation of poorly conductive impurity [53]. From the TOF-SIMs (Fig. 7), which can be confirmed that PANI effectively blocks the accumulation of non-conductive LiF. Moreover, the lower resistance of HEO-MP in EIS (Fig. 5e) shows that less non-conductive components in SEI. Second, PANI can dope HF with quinidine phenyl structure (=N-) to form (=NH^+F^--) to reduce the content of HF and inhibit the dissolution of active material in the literature [54]. Third, PANI effectively promotes the electron transport between materials and encapsulates refined HEO. Therefore, CV measurements at different scan rates (Fig. 4d) confirm that HEO-MP has a more obvious capacitance contribution and excellent high rate performance (Fig. 3d) can be confirmed. It is similar to the result of Sb_2MoO_6 @PANI [52].

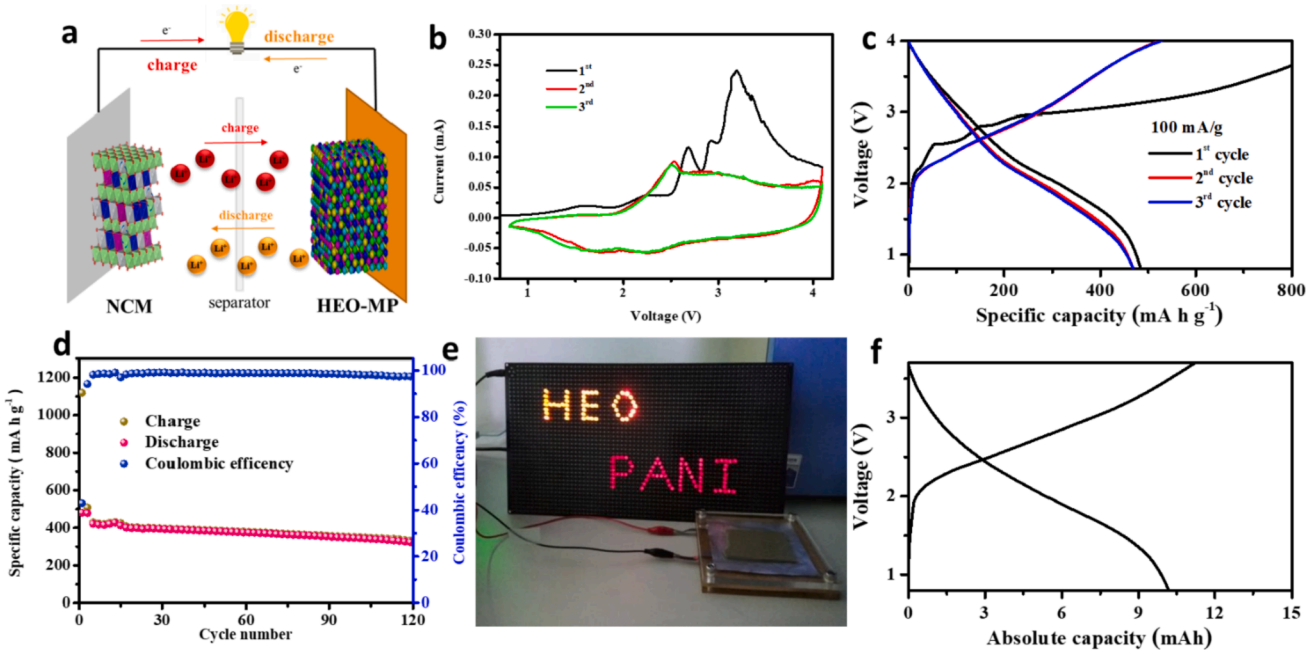

Fig. 8. Electrochemical characterization of HEO-MP //NCM full cells. (a) Schematic of full-cell; (b) The CV curves at 0.1 mV s^{-1}; (c) The charge–discharge curves at 100 mA g^{-1}; (d) Cycling performance at 300 mA g^{-1}; (e) The demonstration of pouch-type battery lighting up; (f) The charge–discharge curves of pouch type full cell under reversible cycling.

To further demonstrate the feasibility of HEO-MP in commercial application, Fig. 8a shows full cell of HEO-MP //NCM. The specific capacity of the full cell is based on the weight of HEO-MP anode. Fig. 8b shows the initial three CV curves of the full cell at a scan rate of 0.1 mV s^{-1}. After the first cycle, the curves of the full cell are similar to HEO-MP half-cell, which means that the full cell exhibits the electrochemical reaction of HEO-MP. Fig. 8c shows voltage profiles of full cell. The third cycle's specific capacity is about 468 mA h g^{-1} at 100 mA g^{-1}. The cycling performance is displayed in Fig. 8d. The capacities of 401 and 329 mA h g^{-1} are maintained after 20 and 120 cycles, respectively, with a capacity fade rate of 0.17% per cycle. In addition, 6 × 6 cm pouch type full cell is fabricated. Fig. 8f shows the charge–discharge curves of the pouch cell under reversible cycling. The capacity of the pouch type full cell is about 10 mA h and successfully lights up 140 LEDs with red and orange color.

4. Conclusions

In summary, we have demonstrated interfacial surface PANI coating on HEO via a simple polymerization method. The flexibility and conductivity of the PANI coating improve electrochemical performance of HEO because it enhances structural stability and inhibits the overgrowth of SEI during cycling. In addition, interface engineering of PANI on HEO significantly improves the reaction and properties between electrodes and electrolytes. When testing the LIB anode, HEO-MP delivers a high reversible capacity of 325 mA h g^{-1} at 10 A $g^{-1}$and excellent cycle performance of 3200 cycles at high current density of 4 A g^{-1}. Moreover, EIS, TOF-SIMS, Ex-situ TEM, SEM and CV confirm that the interface engineering of PANI has the following merits: i) Flexible PANI tightly covers all the cycled HEO electrode to reduce capacity decay and improves cycling stability; ii) PANI blocks direct contact of HEO with electrolyte and buffers volume change to avoid side reactions and overgrowth of SEI; iii) PANI enhances the conductivity of HEO to facilitate electron transport and improve rate performance. Consequently, this work significantly ameliorates the characteristic of HEO through interface engineering which provides new insights into the development of high-entropy materials battery systems and achieves excellent electrochemical properties of high-entropy materials, laying the groundwork for future applications of high-entropy materials.

Declaration of Competing Interest

The authors declare that they have no known competing financial interests or personal relationships that could have appeared to influence the work reported in this paper.

Data availability

No data was used for the research described in the article.

Acknowledgments

We acknowledge the financial support by the Ministry of Science and Technology through the grants of 111-2628-E-007 -008.

Appendix A. Supplementary data

Supplementary data to this article can be found online at https://doi.org/10.1016/j.cej.2022.137924.

References

[1] G.G. Eshetu, H. Zhang, X. Judez, H. Adenusi, M. Armand, S. Passerini, E. Figgemeier, Production of high-energy Li-ion batteries comprising silicon-containing anodes and insertion-type cathodes, Nat. Commun. 12 (2021) 1–14.
[2] M. Armand, J.-M. Tarascon, Building better batteries, nature 451 (2008) 652–657.
[3] P. Poizot, S. Laruelle, S. Grugeon, L. Dupont, J. Tarascon, Nano-sized transition-metal oxides as negative-electrode materials for lithium-ion batteries, Nature 407 (2000) 496–499.
[4] Y. Zhao, X. Li, B. Yan, D. Xiong, D. Li, S. Lawes, X. Sun, Recent developments and understanding of novel mixed transition-metal oxides as anodes in lithium ion batteries, Adv. Energy Mater. 6 (2016) 1502175.
[5] Y. Xu, K. Chu, Z. Li, S. Xu, G. Yao, P. Niu, F. Zheng, Porous CuO@C composite as high-performance anode materials for lithium-ion batteries, Dalton Trans. 49 (2020) 11597–11604.
[6] K. Chu, Z. Li, S. Xu, G. Yao, Y. Xu, P. Niu, F. Zheng, NiO nanocrystals encapsulated into a nitrogen-doped porous carbon matrix as highly stable Li-ion battery anodes, J. Alloys Compd. 854 (2021), 157264.
[7] M. Zheng, H. Tang, L. Li, Q. Hu, L. Zhang, H. Xue, H. Pang, Hierarchically nanostructured transition metal oxides for lithium-ion batteries, Adv. Sci. 5 (2018) 1700592.
[8] J. Cabana L. Monconduit D. Larcher M.R. Palacin Beyond intercalation-based Li-ion batteries: the state of the art and challenges of electrode materials reacting through conversion reactions Adv. Mater. 22 2010 E170 E192.
[9] Y.-Y. Hu, Z. Liu, K.-W. Nam, O.J. Borkiewicz, J. Cheng, X. Hua, M.T. Dunstan, X. Yu, K.M. Wiaderek, L.-S. Du, Origin of additional capacities in metal oxide lithium-ion battery electrodes, Nat. Mater., 12 (2013), pp. 1130-1136.
[10] Q. Li, H. Li, Q. Xia, Z. Hu, Y. Zhu, S. Yan, C. Ge, Q. Zhang, X. Wang, X. Shang, Extra storage capacity in transition metal oxide lithium-ion batteries revealed by in situ magnetometry, Nat. Mater. 20 (2021) 76–83.
[11] C. Ding, L. Wang, W. Zhou, D. Wang, Y. Du, G. Wen, New design on Li-ion battery anode of ternary complex metal/metal oxide@CNT: A case study of hierarchical NiCo-$NiCo_2O_4$@ CNTs, Chem. Eng. J. 353 (2018) 340–349.
[12] L. Shi, D. Li, J. Yu, H.-M. Zhang, S. Ullah, B. Yang, C. Li, C. Zhu, J. Xu, Rational design of hierarchical ZnO@ Carbon nanoflower for high performance lithium ion battery anodes, J. Power Sources 387 (2018) 64–71.
[13] Z.-S. Wu, W. Ren, L. Wen, L. Gao, J. Zhao, Z. Chen, G. Zhou, F. Li, H.-M. Cheng, Graphene anchored with Co_3O_4 nanoparticles as anode of lithium ion batteries with enhanced reversible capacity and cyclic performance, ACS Nano 4 (2010) 3187–3194.
[14] X. Zhou, Z. Dai, S. Liu, J. Bao, Y.G. Guo, Ultra-uniform SnOx/carbon nanohybrids toward advanced lithium-ion battery anodes, Adv. Mater. 26 (2014) 3943–3949.
[15] X. Zhu, Y. Zhu, S. Murali, M.D. Stoller, R.S. Ruoff, Nanostructured reduced graphene oxide/Fe2O3 composite as a high-performance anode material for lithium ion batteries, ACS Nano 5 (2011) 3333–3338.
[16] J.W. Yeh, S.K. Chen, S.J. Lin, J.Y. Gan, T.S. Chin, T.T. Shun, C.H. Tsau, S.Y. Chang, Nanostructured high-entropy alloys with multiple principal elements: novel alloy design concepts and outcomes, Adv. Eng. Mater. 6 (2004) 299–303.
[17] Y. Zhang, T.T. Zuo, Z. Tang, M.C. Gao, K.A. Dahmen, P.K. Liaw, Z.P. Lu, Microstructures and properties of high-entropy alloys, Prog. Mater Sci. 61 (2014) 1–93.
[18] M.-H. Tsai, J.-W. Yeh, High-entropy alloys: a critical review, Mater. Res. Lett. 2 (2014) 107–123.
[19] Y. Ma, Y. Ma, Q. Wang, S. Schweidler, M. Botros, T. Fu, H. Hahn, T. Brezesinski, B. Breitung, High-entropy energy materials: Challenges and new opportunities, Energy Environ. Sci. 14 (2021) 2883–2905.
[20] C.M. Rost, E. Sachet, T. Borman, A. Moballegh, E.C. Dickey, D. Hou, J.L. Jones, S. Curtarolo, J.-P. Maria, Entropy-stabilized oxides, Nat. Commun. 6 (2015) 1–8.
[21] A. Sarkar, L. Velasco, D. Wang, Q. Wang, G. Talasila, L. de Biasi, C. Kübel, T. Brezesinski, S.S. Bhattacharya, H. Hahn, High entropy oxides for reversible energy storage, Nat. Commun. 9 (2018) 1–9.
[22] T.X. Nguyen, J. Patra, J.-K. Chang, J.-M. Ting, High entropy spinel oxide nanoparticles for superior lithiation–delithiation performance, J. Mater. Chem. A 8 (2020) 18963–18973.
[23] K.-H. Tian, C.-Q. Duan, Q. Ma, X.-L. Li, Z.-Y. Wang, H.-Y. Sun, S.-H. Luo, D. Wang, Y.-G. Liu, High-entropy chemistry stabilizing spinel oxide $(CoNiZnXMnLi)_3O_4$ (X= Fe, Cr) for high-performance anode of Li-ion batteries, Rare Met. (2021) 1–11.
[24] Y. Zheng, X. Wu, X. Lan, R. Hu, A Spinel (FeNiCrMnMgAl) 3O4 High Entropy Oxide as a Cycling Stable Anode Material for Li-Ion Batteries, Processes 10 (2022) 49.
[25] K.X. Wang, X.H. Li, J.S. Chen, Surface and interface engineering of electrode materials for lithium-ion batteries, Adv. Mater. 27 (2015) 527–545.
[26] M. Gao, Z. Tang, M. Wu, J. Chen, Y. Xue, X. Guo, Y. Liu, Q. Kong, J. Zhang, Self-supporting N, P doped Si/CNTs/CNFs composites with fiber network for high-performance lithium-ion batteries, J. Alloys Compd. 857 (2021), 157554.
[27] W. Luo, X. Chen, Y. Xia, M. Chen, L. Wang, Q. Wang, W. Li, J. Yang, Surface and interface engineering of silicon-based anode materials for lithium-ion batteries, Adv. Energy Mater. 7 (2017) 1701083.
[28] J. Chen, X. Guo, M. Gao, J. Wang, S. Sun, K. Xue, S. Zhang, Y. Liu, J. Zhang, Self-supporting dual-confined porous Si@c-ZIF@ carbon nanofibers for high-performance lithium-ion batteries, Chem. Commun. 57 (2021) 10580–10583.
[29] G. Yao, P. Niu, Z. Li, Y. Xu, L. Wei, H. Niu, Y. Yang, F. Zheng, Q. Chen, Construction of flexible V_3S_4@ CNF films as long-term stable anodes for sodium-ion batteries, Chem. Eng. J. 423 (2021), 130229.
[30] S. Bhadra, D. Khastgir, N.K. Singha, J.H. Lee, Progress in preparation, processing and applications of polyaniline, Prog. Polym. Sci. 34 (2009) 783–810.
[31] J.M. Jeong, B.G. Choi, S.C. Lee, K.G. Lee, S.J. Chang, Y.K. Han, Y.B. Lee, H.U. Lee, S. Kwon, G. Lee, Hierarchical hollow spheres of Fe_2O_3@ polyaniline for lithium ion battery anodes, Adv. Mater. 25 (2013) 6250–6255.
[32] X. Huang, J. Tu, X. Xia, X. Wang, J. Xiang, Nickel foam-supported porous NiO/polyaniline film as anode for lithium ion batteries, Electrochem. Commun. 10 (2008) 1288–1290.

[33] F. Zhang, H. Cao, D. Yue, J. Zhang, M. Qu, Enhanced anode performances of polyaniline–TiO2–reduced graphene oxide nanocomposites for lithium ion batteries, Inorg. Chem. 51 (2012) 9544–9551.
[34] L. Yi, L. Liu, G. Guo, X. Chen, Y. Zhang, S. Yu, X. Wang, Expanded graphite@ SnO_2@ polyaniline composite with enhanced performance as anode materials for lithium ion batteries, Electrochim. Acta 240 (2017) 63–71.
[35] G. Wang, J. Peng, L. Zhang, J. Zhang, B. Dai, M. Zhu, L. Xia, F. Yu, Two-dimensional SnS_2@ PANI nanoplates with high capacity and excellent stability for lithium-ion batteries, J. Mater. Chem. A 3 (2015) 3659–3666.
[36] L. Hu, Y. Ren, H. Yang, Q. Xu, Fabrication of 3D hierarchical MoS2/polyaniline and MoS_2/C architectures for lithium-ion battery applications, ACS Appl. Mater. Interfaces 6 (2014) 14644–14652.
[37] Y. Dong, Z. Zhao, Z. Wang, Y. Liu, X. Wang, J. Qiu, Dually fixed SnO2 nanoparticles on graphene nanosheets by polyaniline coating for superior lithium storage, ACS Appl. Mater. Interfaces 7 (2015) 2444–2451.
[38] T. Liu, L. Lin, X. Bi, L. Tian, K. Yang, J. Liu, M. Li, Z. Chen, J. Lu, K. Amine, In situ quantification of interphasial chemistry in Li-ion battery, Nat. Nanotechnol. 14 (2019) 50–56.
[39] H.Y. Asl, A. Manthiram, Reining in dissolved transition-metal ions, Science 369 (2020) 140–141.
[40] L. Shen, Q. Che, H. Li, X. Zhang, Mesoporous $NiCo_2O_4$ nanowire arrays grown on carbon textiles as binder-free flexible electrodes for energy storage, Adv. Funct. Mater. 24 (2014) 2630–2637.
[41] J. Jang, J. Ha, J. Cho, Fabrication of water-dispersible polyaniline-poly (4-styrenesulfonate) nanoparticles for inkjet-printed chemical-sensor applications, Adv. Mater. 19 (2007) 1772–1775.
[42] F. Jiang, W. Li, R. Zou, Q. Liu, K. Xu, L. An, J. Hu, MoO_3/PANI coaxial heterostructure nanobelts by in situ polymerization for high performance supercapacitors, Nano Energy 7 (2014) 72–79.
[43] D. Berardan, A. Meena, S. Franger, C. Herrero, N. Dragoe, Controlled Jahn-Teller distortion in (MgCoNiCuZn)O-based high entropy oxides, J. Alloys Compd. 704 (2017) 693–700.
[44] M. Li, Y. Liu, B. Qin, C. Lu, H.A. Butt, T. Zheng, D. Zhang, Polyaniline-coated nanoporous antimony with improved performance for sodium-ion battery anodes, J. Alloys Compd. 861 (2021), 158647.
[45] S. Golczak, A. Kanciurzewska, M. Fahlman, K. Langer, J.J. Langer, Comparative XPS surface study of polyaniline thin films, Solid State Ionics 179 (2008) 2234–2239.
[46] H. Chen, N. Qiu, B. Wu, Z. Yang, S. Sun, Y. Wang, A new spinel high-entropy oxide $(Mg_{0.2}Ti_{0.2}\ Zn_{0.2}Cu_{0.2}Fe_{0.2})_3O_4$ with fast reaction kinetics and excellent stability as an anode material for lithium ion batteries, RSC Advances 10 (2020) 9736–9744.
[47] C. Duan, K. Tian, X. Li, D. Wang, H. Sun, R. Zheng, Z. Wang, Y. Liu, New spinel high-entropy oxides $(FeCoNiCrMnXLi)_3O_4$ (X= Cu, Mg, Zn) as the anode material for lithium-ion batteries, Ceram. Int. 47 (2021) 32025–32032.
[48] M. Kheradmandfard, H. Minouei, N. Tsvetkov, A.K. Vayghan, S.F. Kashani-Bozorg, G. Kim, S.I. Hong, D.-E. Kim, Ultrafast green microwave-assisted synthesis of high-entropy oxide nanoparticles for Li-ion battery applications, Mater. Chem. Phys. 262 (2021), 124265.
[49] T.X. Nguyen, C.-C. Tsai, J. Patra, O. Clemens, J.-K. Chang, J.-M. Ting, Co-free high entropy spinel oxide anode with controlled morphology and crystallinity for outstanding charge/discharge performance in Lithium-ion batteries, Chem. Eng. J. 430 (2022), 132658.
[50] D. Wang, S. Jiang, C. Duan, J. Mao, Y. Dong, K. Dong, Z. Wang, S. Luo, Y. Liu, X. Qi, Spinel-structured high entropy oxide $(FeCoNiCrMn)_3O_4$ as anode towards superior lithium storage performance, J. Alloys Compd. 844 (2020), 156158.
[51] B. Xiao, G. Wu, T. Wang, Z. Wei, Y. Sui, B. Shen, J. Qi, F. Wei, Q. Meng, Y. Ren, High entropy oxides $(FeNiCrMnX)_3O_4$ (X= Zn, Mg) as anode materials for lithium ion batteries, Ceram. Int. 47 (2021) 33972–33977.
[52] L. Yang, H. Liao, Y. Tian, W. Hong, P. Cai, C. Liu, Y. Yang, G. Zou, H. Hou, X. Ji, Rod-Like Sb_2MoO_6: Structure Evolution and Sodium Storage for Sodium-Ion Batteries, Small Methods 3 (2019) 1800533.
[53] H. Jin, S. Xin, C. Chuang, W. Li, H. Wang, J. Zhu, H. Xie, T. Zhang, Y. Wan, Z. Qi, Black phosphorus composites with engineered interfaces for high-rate high-capacity lithium storage, Science 370 (2020) 192–197.
[54] M. Shao, C. Shang, F. Zhang, Z. Xu, W. Hu, Q. Lu, L. Gai, Selective adsorption-involved formation of NMC532/PANI microparticles with high ageing resistance and improved electrochemical performance, J. Energy Chem. 54 (2021) 668–679.